Article

Emergent universal quench dynamics in randomly interacting spin models

Yuchen Li [1,2,13], Tian-Gang Zhou [3,13], Ze Wu[1,2,4,13], Pai Peng [5], Shengyu Zhang[1,2,6], Riqiang Fu [7], Ren Zhang[6,8], Wei Zheng[4,6,9], Pengfei Zhang [10,11 ✉], Hui Zhai [3,6 ✉], Xinhua Peng [1,2,4,6 ✉] & Jiangfeng Du [1,2,4,6,12]

Universal behaviour often emerges in the low-energy equilibrium physics of quantum many-body systems, despite their microscopic differences. Recently, there has been a growing interest in studying the far-from-equilibrium dynamics of quantum many-body systems. Such dynamics usually involve highly excited states beyond the traditional low-energy theory description. Whether universality can also emerge in such non-equilibrium dynamics is the subject of current research. Here, we report the experimental observation of universal dynamics by monitoring the spin depolarization process in a solid-state nuclear magnetic resonance system, described by an ensemble of randomly interacting spins. The spin depolarization can be related to temporal spin–spin correlation functions at high temperatures. We discover that these correlation functions obey a universal functional form. This finding helps us identify the dominant interacting processes in the spin depolarization dynamics that lead to universality. Our observation demonstrates the existence of universality even in non-equilibrium dynamics at high temperatures, thereby complementing the well-established universality in low-energy physics.

Universality refers to when a set of simple rules and a small number of parameters can universally describe a physical phenomenon across various systems, despite their complicated and distinct microscopic details. Numerous examples have demonstrated that universal behaviours can occur in different subfields of physics. For examples, in atomic physics, a single parameter, the *s*-wave scattering length, governs the low-energy scattering between two atoms[1,2]. In other words, regardless of the specific atomic species with different interatomic Van der Waals potentials, their low-energy interaction properties tend to be

identical as long as their *s*-wave scattering lengths are the same. Similarly, in condensed matter physics, systems within the quantum critical regime exhibit identical low-energy properties if they belong to the same universality class, even though their microscopic Hamiltonians can be vastly different[3].

However, most known examples of universal behaviours occur in low-energy physics. In contrast, far-from-equilibrium quantum dynamics always involves highly excited states. In particular, we often study a type of quench dynamics where we start with an initial state at

[1]CAS Key Laboratory of Microscale Magnetic Resonance and School of Physical Sciences, University of Science and Technology of China, Hefei, China. [2]Anhui Province Key Laboratory of Scientific Instrument Development and Application, University of Science and Technology of China, Hefei, China. [3]Institute for Advanced Study, Tsinghua University, Beijing, China. [4]CAS Center for Excellence in Quantum Information and Quantum Physics, University of Science and Technology of China, Hefei, China. [5]Frontiers Science Center for Nano-optoelectronics, School of Physics, Peking University, Beijing, China. [6]Hefei National Laboratory, Hefei, China. [7]National High Magnetic Field Laboratory, Tallahassee, FL, USA. [8]School of Physics, Xi'an Jiaotong University, Xi'an, China. [9]Hefei National Research Center for Physical Sciences at the Microscale and School of Physical Sciences, University of Science and Technology of China, Hefei, China. [10]Department of Physics, Fudan University, Shanghai, China. [11]Shanghai Qi Zhi Institute, Shanghai, China. [12]Institute of Quantum Sensing and School of Physics, Zhejiang University, Hangzhou, China. [13]These authors contributed equally: Yuchen Li, Tian-Gang Zhou, Ze Wu. ✉e-mail: pengfeizhang.physics@gmail.com; hzhai@tsinghua.edu.cn; xhpeng@ustc.edu.cn

high temperature and follow its unitary evolution, which is governed by a quantum many-body Hamiltonian, such as cold atoms[4,5], ions[6,7], nitrogen-vacancy centres[8,9] and nuclear magnetic resonance (NMR) systems[10–21]. Such dynamics can be attributed to temporal correlation functions at infinite temperatures[4–13,15,18–30]. Discovering universality in such dynamics complements established universality in low-energy equilibrium physics. So far, such examples are still rare. A recent experiment in a cold-atom system has revealed universal Kardar–Parisi–Zhang scaling for such quench dynamics in an integrable spin chain[4]. In contrast, in this article, we study spin models with random and all-to-all interactions using a solid-state NMR system. We reveal a couple of universal parameters in this system that can capture the main features of the quench dynamics, including both spin depolarization dynamics and multiple quantum coherence (MQC). Our findings represent substantial progress in alignment with previous work on the dynamical behaviours of NMR spin systems[10–12,22,23].

To be concrete, let us consider an initial density matrix $\hat{\rho} \propto \mathbb{1} + \epsilon \hat{O}$, where ϵ is a small parameter and $\hat{O}$ is a traceless operator as a perturbation to the infinite-temperature ensemble. This density matrix undergoes time evolution governed by a quantum many-body Hamiltonian $\hat{H}$, given by $\hat{\rho}(t) = e^{-i\hat{H}t/\hbar} \hat{\rho} e^{i\hat{H}t/\hbar}$. Then, by measuring the expectation value of operator $\hat{O}$ at varying evolution time, we can access the autocorrelation function as $\langle\hat{O}(t)\rangle = \text{Tr}[\hat{O}\hat{\rho}(t)] \propto \mathcal{C}(t)$, where $\mathcal{C}(t) = \frac{1}{c_O}\text{Tr}[\hat{O}(t)\hat{O}(0)]$ is the autocorrelation function with normalization constant c_O such that $\mathcal{C}(0) = 1$. This autocorrelation function is defined at infinite temperatures because it equally incorporates contributions from all eigenstates, thereby reflecting the properties of the many-body Hamiltonian. During the Heisenberg evolution, the operator complexity of $\hat{O}(t)$ continuously increases[31,32], resulting in $\mathcal{C}(t)$ decaying. Therefore, the universality observed in $\mathcal{C}(t)$ ultimately stems from the universal behaviour in the complexity theory of operator growth[24].

Our experiments were conducted on a powder sample of adamantane ($C_{10}H_{16}$)[14,19,33–35]. Each adamantane molecule contains 16 hydrogen atoms (^1H), and each ^1H carries nuclear spin $S = 1/2$. There are approximately 10^9 to 10^{12} molecules contained in a single granule of the powder, which has a size of the order of micrometres (Fig. 1a). These spins interact with each other through magnetic dipolar interactions. The sample was placed in a uniform magnetic field $B_0 = 9.4$ T along the $\hat{z}$ direction. Therefore, the Hamiltonian reads

$$\hat{H} = -\hbar\gamma_H B_0 \sum_{ia} \hat{S}_{ia}^z$$
$$+ \sum_{(i,a)<(j,b)} \frac{\mu_0 \hbar^2 \gamma_H^2}{4\pi r_{ia,jb}^3}\left[\hat{\mathbf{S}}_{ia} \cdot \hat{\mathbf{S}}_{jb} - \frac{3(\hat{\mathbf{S}}_{ia} \cdot \mathbf{r}_{ia,jb})(\hat{\mathbf{S}}_{jb} \cdot \mathbf{r}_{ia,jb})}{r_{ia,jb}^2}\right], \quad (1)$$

where $\hat{\mathbf{S}}_{ia} = (\hat{S}_{ia}^x, \hat{S}_{ia}^y, \hat{S}_{ia}^z)$ are the spin operators for each ^1H. i and j label molecules positioned on a face-centred cubic lattice (Fig. 1b). The indices $a, b = 1, \ldots, 16$ label the spin-1/2 within each molecule. The constraint $(i, a) < (j, b)$ is defined as $a < b$ when $i = j$ and otherwise $i < j$. μ_0 is the vacuum magnetic permeability and γ_H is the proton's gyromagnetic ratio. $\mathbf{r}_{ia,jb} = \mathbf{R}_{ij} + \mathbf{l}_a - \mathbf{l}_b$ and $r_{ia,jb} = |\mathbf{r}_{ia,jb}|$, where $\mathbf{R}_{ij}$ denotes the displacement between the centres of two molecules. $\mathbf{l}_a$ and $\mathbf{l}_b$ are the vectors from the centre of a molecule to each nuclear spin carrier ^1H. $\gamma_H B_0$ represents the strength of the Zeeman splitting resulting from the external magnetic field.

At room temperature, each molecule undergoes rapid rotation around its centre due to thermal motion, with a characteristic timescale of 10^{-11} s (Fig. 1c)[36]. This timescale is much faster than the timescale of a dipolar interaction, which is approximately 10^{-3} s. By averaging the Hamiltonian over the solid angles $\mathbf{l}_a$ and $\mathbf{l}_b$ and to the leading-order approximation, the Hamiltonian of equation (1) becomes[36–38]

$$\hat{H} = \sum_{i<j,ab} \frac{\mu_0 \hbar^2 \gamma_H^2}{4\pi R_{ij}^3}\left[\hat{\mathbf{S}}_{ia} \cdot \hat{\mathbf{S}}_{jb} - \frac{3(\hat{\mathbf{S}}_{ia} \cdot \mathbf{R}_{ij})(\hat{\mathbf{S}}_{jb} \cdot \mathbf{R}_{ij})}{R_{ij}^2}\right] - \hbar\gamma_H B_0 \sum_{ia} \hat{S}_{ia}^z. \quad (2)$$
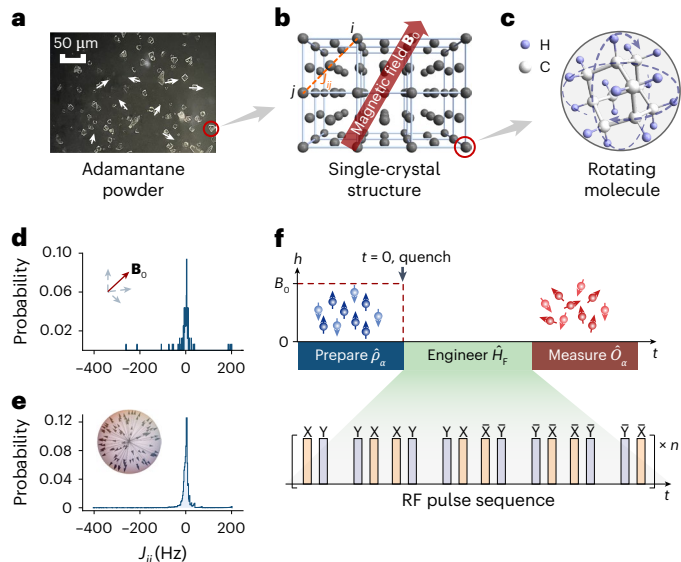
Fig. 1 | Experimental protocol. a, Microscopic picture of powder sample of adamantane ($C_{10}H_{16}$). The granules, whose sizes are of the order of micrometres, exhibit random orientations. **b,** In one granule, the adamantane molecules form a face-centred cubic lattice. The orientation of the static magnetic field $\mathbf{B}_0$ relative to the lattice principal axes determines the values of the secular dipolar coupling strength J_{ij}. **c,** Each molecule undergoes rapid rotation around its lattice site due to thermal motion. The lattice site effectively serves as a time-averaged position for all the nuclear spins within the same molecule. ^1H carries nuclear spin-1/2 and ^{12}C carries no spin. **d,e,** Probability distributions of the intermolecular coupling J_{ij}, for a given orientation of $\mathbf{B}_0$ (**d**) and for the distribution averaged over 10^5 random orientations denoted by arrows in the spherical surface (**e**). Up to the 13th neighbour couplings were incorporated in the calculation. **f,** Experimental protocol of the quench dynamics. First, we prepared a polarized initial density matrix $\hat{\rho}_\alpha \propto \mathbb{1} + \epsilon \sum_{ia} \hat{S}_{ia}^\alpha$, $\alpha = \hat{x}$, $\hat{y}$ or $\hat{z}$. Then, the state evolved under the anisotropic random spin models engineered by the RF pulse sequence illustrated below and also used in refs. 17–21,40, after which we measured the magnetization $\hat{O}_\alpha = \sum_{ia} \hat{S}_{ia}^\alpha$.

Thus, a nuclear spin in one molecule interacts identically with any other nuclear spin in another molecule.

Furthermore, the presence of an external magnetic field causes all spins to rotate along the $\hat{z}$ direction with a characteristic timescale of 10^{-9} s. This rapid motion can be effectively eliminated by applying a unitary transformation $\exp(-i\gamma_H B_0 \sum_{ia} \hat{S}_{ia}^z t)$. After taking the secular approximation[39], we obtain the Hamiltonian

$$\hat{H} = \hbar \sum_{i<j,ab} J_{ij}\left(-\hat{S}_{ia}^x\hat{S}_{jb}^x - \hat{S}_{ia}^y\hat{S}_{jb}^y + 2\hat{S}_{ia}^z\hat{S}_{jb}^z\right), \quad (3)$$

where $J_{ij} \equiv (\mu_0/4\pi)(\hbar\gamma_H^2/2R_{ij}^3)(1 - 3\cos^2\theta_{ij})$. θ_{ij} represents the angle between $\mathbf{R}_{ij}$ and the $\hat{z}$ direction. Now, randomness arises because the molecules occupy lattice sites, and in a powder sample, the orientations between the lattice axes and the $\hat{z}$ direction are random. Figure 1d,e presents the probability distributions of J_{ij} calculated from the lattice structure. It demonstrates that J_{ij} can be regarded as random variables, with a mean and variance satisfying $\overline{J_{ij}} = 0$ and $\overline{J_{ij}^2} = 4J^2/N$. $N = N_m N_a$ is the total number of spins, in which N_m is the number of molecules and $N_a = 16$ represents the number of ^1H in each molecule. We calibrated J within the range $2\pi[1432, 1502]$ Hz (Supplementary Note 2), with an average value $\bar{J} = (2\pi)\,1{,}460$ Hz, which is used later in the notation for the dimensionless timescale $\bar{J}t$.

Next, by periodically applying a radio-frequency (RF) pulse sequence, as shown in Fig. 1f (refs. 17–21,40), the Hamiltonian in

equation (3) can be further engineered into a more general form according to the average Hamiltonian theory[41]

$$\hat{H} = \hbar \sum_{i<j,ab} J_{ij} \left(\xi_x \hat{S}_{ia}^x \hat{S}_{jb}^x + \xi_y \hat{S}_{ia}^y \hat{S}_{jb}^y + \xi_z \hat{S}_{ia}^z \hat{S}_{jb}^z \right) + \dots \qquad (4)$$

Here ξ_α ($\alpha = \hat{x}, \hat{y}, \hat{z}$) represents three anisotropic parameters that are subjected to a constraint $\sum_\alpha \xi_\alpha = 0$, which is inherited from the Hamiltonian of equation (3) and conserved under global rotations. Note that the measurement is summed over random crystalline orientations, which facilitates equation (4), a random spin model in the sense of ensemble average. The various configurations of (ξ_x, ξ_y, ξ_z) can be achieved by manipulating the pulse intervals (Methods and Supplementary Information). The Floquet-engineered random spin model in equation (4) is not integrable and generically prethermalizes an initial state with finite energy to quasi-equilibrium, which can be characterized by a canonical ensemble $\hat{\rho}_{\text{pre}} = e^{-\beta \hat{H}}/\mathcal{Z}$, where $\mathcal{Z}$ is the partition function and β is determined by the initial-state energy[18,20,42–44]. The Hamiltonian information is, thus, inherited by the prethermal state $\hat{\rho}_{\text{pre}}$, which can be learned from state tomography (Methods and Supplementary Information). Deviations from the target Hamiltonian configurations were calibrated to be within 3%. The term ... in equation (4) represents residual terms other than $\hat{S}_{ia}^\alpha \hat{S}_{jb}^\alpha$, and the total weight of these terms was calibrated to be less than 20%.

In the experiment, we considered three different initial density matrices, denoted as $\hat{\rho}_\alpha \propto \mathbb{1} + \epsilon \hat{O}_\alpha$. Here, $\hat{O}_\alpha = \sum_{ia} \hat{S}_{ia}^\alpha$ ($\alpha = \hat{x}, \hat{y}$ or $\hat{z}$) represents the total spin along different directions, and $\epsilon \approx 6.4 \times 10^{-5}$. We evolved the initial density matrix under the Hamiltonian of equation (4). Subsequently, we measured $\langle \hat{O}_\alpha(t) \rangle$. As discussed earlier, the result corresponds to the normalized autocorrelation function $\mathcal{C}_\alpha(t)$. The most notable finding of this experiment is the discovery of a universal functional form for $\mathcal{C}_\alpha(t)$. Specifically, for $\alpha = \hat{x}$, we introduce two quantities, namely, W_x and Γ, which are quadratic polynomials of the microscopic parameters ξ_α proposed in ref. [45]:

$$W_x \equiv -\xi_x^2 + \xi_y^2 - 4\xi_y\xi_z + \xi_z^2, \qquad (5)$$

$$\Gamma \equiv \xi_x^2 + \xi_y^2 + \xi_z^2. \qquad (6)$$

Using these two polynomials, we introduced two characteristic energy scales $\hbar\omega_x \equiv c\hbar\sqrt{|W_x|}J$ and $\hbar\lambda \equiv c\hbar\sqrt{\Gamma}J$. Here c is an $o(1)$ constant. For $\alpha = \hat{y}$ or $\alpha = \hat{z}$, we introduced W_y and W_z through permutations as $W_y = -\xi_y^2 + \xi_z^2 - 4\xi_z\xi_x + \xi_x^2$ and $W_z = -\xi_z^2 + \xi_x^2 - 4\xi_x\xi_y + \xi_y^2$. $\hbar\omega_y$ and $\hbar\omega_z$ were then defined correspondingly. We found that $\mathcal{C}_\alpha(t)$ can be described well by

$$\begin{cases} a\cos(\omega_\alpha t + \phi)\,e^{-\lambda t}, & \text{if } W_\alpha > 0, \\ a\cosh(\omega_\alpha t + \phi)\,e^{-\lambda t} \approx a'\,e^{-(\lambda - \omega_\alpha)t}, & \text{if } W_\alpha < 0, \end{cases} \qquad (7)$$

where a, a' and ϕ are non-universal constants. This functional form was motivated by a quasinormal mode analysis for non-equilibrium dynamics. Quasinormal modes are collective modes with complex frequencies $\omega_a - i\lambda_a$, which govern the dynamically oscillatory and decaying response in strongly interacting systems[46,47]. Here, a labels different modes. In the long-time limit, we retained only the mode with the smallest λ_a, resulting in the functional form proposed in equation (7) (see 'Large-M expansion' in Methods and Supplementary Note 6B for a detailed derivation). Our results reveal the universal scaling functions between (ω_a, λ) and the microscopic parameters in the Hamiltonian. As a consequence, this framework easily enables the establishment of a precise criterion for determining the presence of oscillatory or monotonic decay in spin relaxation dynamics. By offering a quantitative understanding, this advance marks a notable step forward in alignment with previous research[10–12,22,23]. However, despite the effectiveness and simplicity of equation (7), it leads to larger deviations from the experimental data around the transition point $W_\alpha = 0$, where the multi-mode dynamics become more evident.

Equation (7) is confirmed by the experimental data presented in Fig. 2. We polarized the system initially in three different directions $\alpha = \hat{x}, \hat{y}, \hat{z}$ respectively and then measured $\langle \hat{O}_\alpha \rangle$ for $\xi_z = 0.2$ and $\xi_x \in [-0.4, 0.2]$. The spin depolarization dynamics of $\langle \hat{O}_\alpha \rangle$ are depicted in Fig. 2a–c. We fitted these curves using the function $A\cos(\Omega t + \Phi)\,e^{-\Lambda t}$ and obtained Ω and Λ for each case. Importantly, this approach does not assume the existence of an oscillating-to-monotonic transition. Comparing with equation (7), we predicted $(\Omega, \Lambda) = (\omega_\alpha, \lambda)$ when $W_\alpha > 0$, whereas $(\Omega, \Lambda) = (0, \lambda - \omega_\alpha)$ when $W_\alpha < 0$.

Given the constraint $\sum_\alpha \xi_\alpha = 0$, we have $W_x = -6\xi_y\xi_z$, $W_y = -6\xi_z\xi_x$ and $W_z = -6\xi_x\xi_y$. In this experiment, we fixed $\xi_z = 0.2$. Thus, when $\alpha = \hat{x}$, we found $W_x = 1.2(0.2 + \xi_x) > 0$ for $\xi_x > -0.2$. As shown in Fig. 2a,d, the autocorrelation function oscillated when $\xi_x > -0.2$, and the frequency $\Omega/\bar{J}$ scaled as $c\sqrt{W_x}$, where $\bar{J}$ is the average value of J determined experimentally. Figure 2g demonstrates that $\Lambda/\bar{J}$ scaled with $c\sqrt{\Gamma}$ for $\xi_x > -0.2$ and scaled with $c(\sqrt{\Gamma} - \sqrt{-W_x})$ for $\xi_x < -0.2$. From the fitting, we obtained $c = 0.91(7)$. Similarly, for $\alpha = \hat{y}$, we have $W_y = -1.2\xi_x > 0$ for $\xi_x < 0$, where the frequency $\Omega/\bar{J}$ is fitted by $c\sqrt{W_y}$ and $\Lambda/\bar{J}$ by $c\sqrt{\Gamma}$. For $\xi_x > 0$, the frequency was zero, and $\Lambda/\bar{J}$ was fitted by $c(\sqrt{\Gamma} - \sqrt{-W_y})$. The fitting gave $c = 0.91(7)$, as shown in Fig. 2b,e,h. For $\alpha = \hat{z}$, $W_z = 6\xi_x(0.2 + \xi_x) > 0$ for $\xi_x > 0$ or $\xi_x < -0.2$, where the frequency was fitted by $c\sqrt{W_z}$ and $\Lambda/\bar{J}$ by $c\sqrt{\Gamma}$. For $-0.2 < \xi_x < 0$, the frequency was zero, and $\Lambda/\bar{J}$ was fitted by $c(\sqrt{\Gamma} - \sqrt{-W_z})$. The fittings yielded $c = 0.87(10)$, as shown in Fig. 2c,f,i. The constants c obtained from the three fittings are consistent with each other within the error bars.

As a check of self-consistency, note that when $\Gamma = -W_x$, then $\Lambda = 0$, and our ansatz shows that $\mathcal{C}_x(t)$ does not decay at all. Observe that $\Gamma = -W_x$ implies $\xi_y = \xi_z$, and the system restores spin rotational symmetry along $\hat{x}$. Therefore, $\hat{O}_x$ commutes with the Hamiltonian, and the total spin along $\hat{x}$ should not evolve in time. Similar conditions hold for $\alpha = \hat{y}$ and $\hat{z}$. This observation is also consistent with our experimental findings, indicating that our system remained coherent and that decoherence was negligible within the experimental timescale. Furthermore, this scaling behaviour has been confirmed by exact-diagonalization calculations and approximation methods such as large-M expansion and mean-field theory (see the Methods for further details)[45]. Each theoretical approach has its own advantages and disadvantages. The exact-diagonalization method captures the exact non-equilibrium quantum dynamics for SU(2) spin but only for small system size N. The semiclassical method captures the non-equilibrium spin dynamics through the Landau–Lifshitz equation of the non-equilibrium dynamics for intermediate system size N. The large-M expansion captures the leading-order contribution to non-equilibrium dynamics for large system size N, which is rigorous at large M for SU(2) × SU(M) spin. Notably, the same combinations of the anisotropic parameters in the Hamiltonian enter the non-equilibrium dynamics, leading to the universal polynomial scaling of the oscillation frequency and decay rate. Figure 3a,b compares Ω and Λ obtained by these three theoretical methods with the experimental data, showing the good agreement. All the theoretical results obey the universal function form shown in equations (5)–(7) but with slightly different values of c.

Below, we will discuss some physical intuitions as to why the quantities W_α and Γ emerge as universal parameters in the quench dynamics. In low-energy physics, universality arises when a specific set of diagrams becomes the most relevant and dominates the physical process under consideration, for instance, near a symmetry-breaking phase-transition point in the Landau paradigm[48]. In our case, we argue that the same reasoning applies to the emergence of universality in quench dynamics, albeit with a focus on the infinite-temperature autocorrelation function $\mathcal{C}_\alpha(t)$.

Without loss of generality, we consider $\alpha = \hat{x}$ and the correlation function $\mathcal{C}_x(t) = \frac{1}{c_0} \sum_{ij,ab} \langle \hat{S}_{ia}^x(t) \hat{S}_{jb}^x(0) \rangle$. The experimental result suggests that the dominant contributions to $\langle \hat{S}_{ia}^x(t) \hat{S}_{jb}^x(0) \rangle$ contain a few
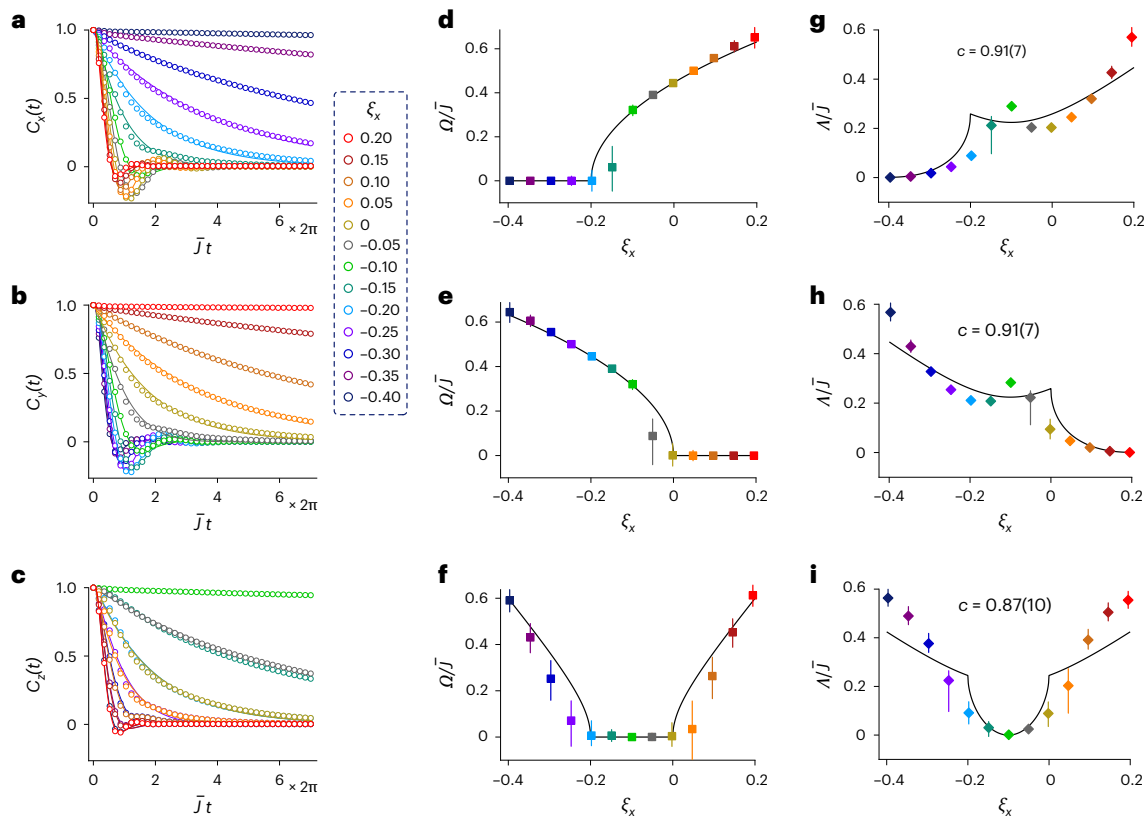
Fig. 2 | Dynamical evolution of spin polarization during the quench dynamics. a–c, Experimental measurements of $C_\alpha(t) \propto \langle \hat{O}_\alpha \rangle$, with $\hat{O}_\alpha = \sum_{ia} \hat{S}_{ia}^\alpha$. The data were normalized by the value at $t = 0$. Error bars (~10^{-4}) are incorporated within the markers of the data points to represent the 95% confidence intervals determined from read-out noise (Supplementary Fig. 2a). The initial-state density matrix was prepared as $\hat{\rho}_\alpha \propto \mathbb{1} + \epsilon \hat{O}_\alpha$. We have $\alpha = \hat{x}$ (**a**), $\alpha = \hat{y}$ (**b**) and $\alpha = \hat{z}$ (**c**). We fixed $\xi_z = 0.2$ and $\sum_\alpha \xi_\alpha = 0$ in the Hamiltonian of equation (4). The colours denote the different values of ξ_x, which vary from -0.4 to 0.2. The solid lines represent the fittings using a general function $A\cos(\Omega t + \Phi)\exp(-\Lambda t)$, from which both Ω and Λ were obtained. **d–f**, Oscillation frequencies $\Omega/\bar{J}$

extracted from **a–c** plotted as a function of ξ_x for $\alpha = \hat{x}$ (**d**), $\hat{y}$ (**e**) and $\hat{z}$ (**f**). The solid lines denote zero when $W_\alpha < 0$ and fits $c\sqrt{W_\alpha}$ for $W_\alpha > 0$. **g–i**, $\Lambda/\bar{J}$ extracted from **a–c** plotted as a function of ξ_x for $\alpha = \hat{x}$ (**g**), $\hat{y}$ (**h**) and $\hat{z}$ (**i**). The solid lines are fits $c\sqrt{\Gamma}$ when $W_\alpha > 0$ and fits $c(\sqrt{\Gamma} - \sqrt{-W_\alpha})$ for $W_\alpha < 0$. The constant c was obtained from simultaneous fitting of both $\Omega/\bar{J}$ and $\Lambda/\bar{J}$. The 95% confidence intervals are given in parentheses. The error bars for data points in **d–i** include both the 95% confidence intervals estimated from the fitting residuals and the fluctuation due to varying the fitting range (from 15 to 41 points). This strategy reduced the fitting error caused by the ambiguity of the fitting range, thereby enhancing the reliability of the fitting results.

interaction channels, which can be identified by examining the terms $\langle \hat{H}\hat{S}_{ia}^x \hat{H}\hat{S}_{jb}^x \rangle$ and $\langle \hat{H}^2 \hat{S}_{ia}^x \hat{S}_{jb}^x \rangle$ (Supplementary Note 6E). This argument can be justified with large-M theory and mean-field theory[45], which are two of the most popular approximation schemes for studying spin models. The large-M expansion has been particularly successful for studying a randomly interacting spin model known as the Sachdev–Ye model[49], which was later extended to the celebrated Sachdev-Ye-Kitaev model[50–52]. These two terms are illustrated by the Feynman diagrams in Fig. 3c–f, with contributions from $i = j$ given in Fig. 3c,d, and contributions from $i \neq j$ given in Fig. 3e,f. Lengthy but straightforward calculations demonstrate that the contribution from diagram Fig. 3c is exactly proportional to Γ as defined in equation (6), whereas the contributions from diagrams Fig. 3d–f can be combined into W_x as defined in equation (5) (Supplementary Note 6E). That the experimental data can be captured well by these parameters reveals the underlying physics behind the dynamics, indicating that this non-equilibrium process is dominated by the interaction processes shown in Fig. 3.

This universal behaviour can also be applied to similar models realized in other physical systems. As a concrete example, a similar random spin model has been realized by Rydberg atoms excited in an ultracold atomic gas, and a non-monotonic dependence of the relaxation dynamics on the anisotropic parameter ratio was observed[5]. This dependence also aligns with the dependency of the decay rate on the anisotropic parameters presented in this work.

For a given direction α, whether $W_\alpha > 0$ or $W_\alpha < 0$ not only distinguishes two types of quench dynamics for the two-point correlator but also marks the difference in higher-order correlators. We now investigate the higher-order correlation by studying MQCs[53–58]. The experimental protocol, as described in refs. 57,58, was used to extract the MQC spectrum by using its relation with the out-of-time-order (OTO) correlator $F(\phi, t) = \frac{1}{c_O} \mathrm{Tr}[e^{-i\hat{O}_\alpha\phi} \hat{O}_\alpha(t) e^{i\hat{O}_\alpha\phi} \hat{O}_\alpha(t)]$ (refs. 6,15,59–65). $F(\phi, t)$ can be expanded as $F(\phi, t) = \sum_m I_m^{(\alpha)}(t) e^{-im\phi}$, where $I_m^{(\alpha)}$ represents the intensity of the mth-order quantum coherences in the eigenbasis of $\hat{O}_\alpha$. $I_0^{(\alpha)}$ incorporates both the zero-quantum coherences and populations (diagonal elements).

In this protocol, we first evolved $\hat{\rho}_\alpha$ with the many-body Hamiltonian $\hat{H}$ for a time duration t. Then, we applied a spin rotation with angle ϕ given by $\exp(-i\hat{O}_\alpha\phi)$. This was followed by another evolution under the Hamiltonian $-\hat{H}$ for the same time duration t. Afterwards, we measured the expectation value $\langle \hat{O}_\alpha \rangle$. Like the measurement of the autocorrelation function, this protocol allowed us to measure the OTO correlator $F(\phi, t)$, as

$$\langle \hat{O}_\alpha \rangle = \mathrm{Tr}[e^{i\hat{H}t/\hbar} e^{-i\hat{O}_\alpha\phi} e^{-i\hat{H}t/\hbar} \hat{\rho}_\alpha e^{i\hat{H}t/\hbar} e^{i\hat{O}_\alpha\phi} e^{-i\hat{H}t/\hbar} \hat{O}_\alpha]$$

$$= \mathrm{Tr}[e^{-i\hat{O}_\alpha\phi} \hat{\rho}_\alpha(t) e^{i\hat{O}_\alpha\phi} \hat{O}_\alpha(t)] \qquad (8)$$

$$\propto F(\phi, t).$$
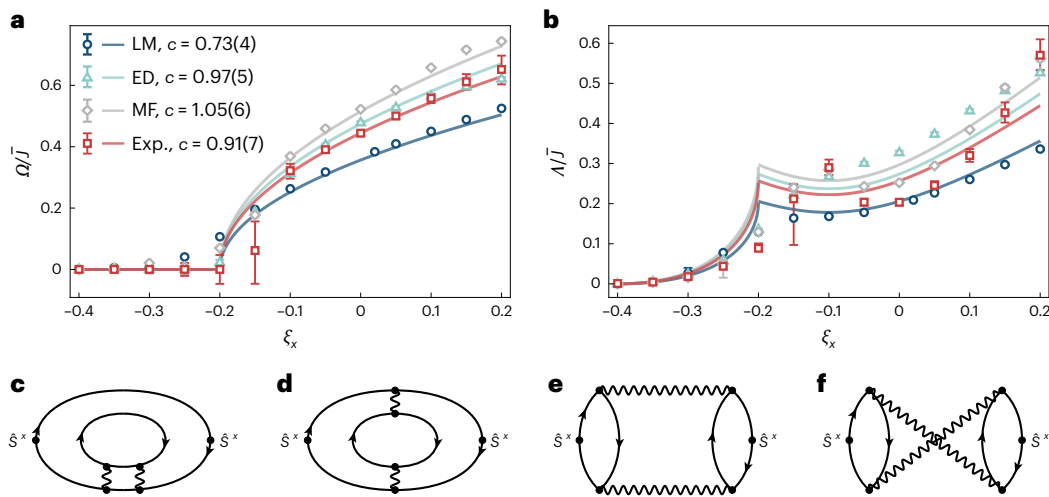
Fig. 3 | Theoretical results and diagrammatic analysis. a,b, Frequency (**a**) and decay rate (**b**) obtained from the large-M expansion (LM), exact diagonalization (ED), mean-field theory (MF) and the experimental data (Exp.), which are represented by different colours. The error bars include both the 95% confidence intervals estimated from the fitting residuals and the fluctuations due to varying the fitting range. The solid lines are simultaneous fittings of the frequency $\Omega/\bar{J}$ and the decay rate $\Lambda/\bar{J}$ using their theoretical piecewise functions determined from equation (7): $(\Omega, \Lambda)/\bar{J} = c(\sqrt{W_x}, \sqrt{\Gamma})$ when $W_x > 0$ and $(\Omega, \Lambda)/\bar{J} = c(0, \sqrt{\Gamma} - \sqrt{-W_x})$ when $W_x < 0$. The uncertainties of the constants c in the parentheses denote the 95% confidence intervals. **c–f,** These four diagrams represent contributions from $\sum_{i,a} \text{Tr}[\hat{H}^2 \hat{S}_{ia}^x \hat{S}_{ia}^x]$ (**c**), $\sum_{i,a} \text{Tr}[\hat{H}\hat{S}_{ia}^x \hat{H}\hat{S}_{ia}^x]$ (**d**), $\sum_{(i,a)\neq(j,b)} \text{Tr}[\hat{H}\hat{S}_{ia}^x \hat{H}\hat{S}_{jb}^x]$ (**e**) and $\sum_{(i,a)\neq(j,b)} \text{Tr}[\hat{H}^2 \hat{S}_{ia}^x \hat{S}_{jb}^x]$ (**f**). In each diagram, the dots represent spin operators. Two of these are labelled as $\hat{S}^x$ as they are the corresponding operators in the two-point correlator. The loops represent the trace of spin operators, whereas the arrows indicate the order of spin operator contractions. The wavy lines and their associated dots denote the vertices of random spin interactions.

Then, by varying the rotation angle ϕ and time duration t and subsequently applying a Fourier transform with respect to ϕ, the MQC spectrum $\{I_m^{(\alpha)}(t)\}$ was obtained. Note that

$$\partial^2 F(\phi,t)/\partial\phi^2|_{\phi=0} = -\sum_m I_m^{(\alpha)}(t)m^2 = \frac{1}{c_O}\text{Tr}([\hat{O}_\alpha(t), \hat{O}_\alpha]^2),$$

the OTO commutator[59]. This connection between MQC and the OTO commutator[59] allowed us to characterize information scrambling in the system[59].

Figure 4 shows the results for $I_m^{(\alpha)}(t)$ for two cases with $\alpha = \hat{z}$. Figure 4a depicts the case with $(\xi_x, \xi_y, \xi_z) = (-0.125, -0.025, 0.15)$ and $W_z = -0.01875 < 0$. In this scenario, we observed a monotonic decay of $I_0^{(z)}$, with its weight gradually spreading into higher-order quantum coherences. Figure 4b illustrates the case with $(\xi_x, \xi_y, \xi_z) = (-0.1, 0.1, 0)$ and $W_z = 0.06 > 0$. In this situation, clear oscillations were observed for both $I_0^{(z)}(t)$ and $I_{\pm2}^{(z)}(t)$. Besides, it seems that $I_0^{(z)}(t)$ and $I_{\pm2}^{(z)}(t)$ oscillated with a frequency roughly double that of $\mathcal{C}_z(t)$, as indicated by the time points when $I_0^{(z)}(t)$, $I_{\pm2}^{(z)}(t)$ and $\mathcal{C}_z(t)$ reached their initial trough or peak: $\bar{J}t_{\text{dip}}^{(I)}/2\pi \approx 1.29$, $\bar{J}t_{\text{peak}}^{(I)}/2\pi \approx 1.22$ and $\bar{J}t_{\text{dip}}^{(e)}/2\pi \approx 2.37$. This is reasonable considering that the OTO commutator $\text{Tr}([\hat{O}_z(t), \hat{O}_z]^2)$ involves a square of $\hat{O}_z(t)\hat{O}_z$. This observation was verified by varying the Hamiltonian configurations (Supplementary Information), and it demonstrates the emergence of universality in a complementary aspect of quantum dynamics beyond autocorrelation functions.

To conclude, we experimentally studied the far-from-equilibrium quench dynamics in randomly interacting spin models using solid-state NMR systems. The mean strength of the random interaction was the only energy scale in the Hamiltonian governing the dynamics. Hence, this problem is intrinsically a strongly interacting many-body problem that lacks small perturbation parameters. Developing a physical understanding of such a system at non-equilibrium is one of the most challenging problems. Numerical methods, like exact diagonalization, are limited to systems much smaller than the actual physical system and do not provide insightful physical intuitions. Approximation schemes, such as large-M theory, do provide helpful intuition but involve uncontrolled errors. In light of these challenges, quantitative
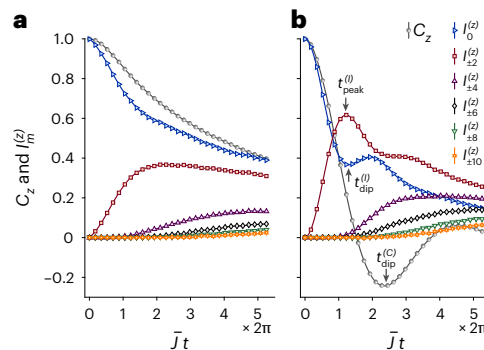
Fig. 4 | MQCs for randomly interacting spin models. a,b, MQC intensities of different orders in the eigenbasis of $\hat{O}_z$, denoted as $I_m^{(z)}$, depicted as functions of the evolution time $\bar{J}t$. The values of (ξ_x, ξ_y, ξ_z) were $(-0.125, -0.025, 0.15)$ (**a**) and $(-0.1, 0.1, 0)$ (**b**). At each time $\bar{J}t$, the data were normalized by $F(\phi,t)|_{\phi=0} = \sum_m I_m^{(z)}(t)$ to ensure that $\sum_m I_m^{(z)}(t) = 1$. The different curves are for various values of the coherence order m. The error bars ($\sim 10^{-4}$) incorporated within the markers of the data points represent the 95% confidence intervals determined from read-out noise (Supplementary Fig. 2a). The solid lines denote the cubic spline interpolations. From **b**, we found that $I_0^{(z)}(t)$ reached its initial trough at $\bar{J}t_{\text{dip}}^{(I)}/2\pi \approx 1.29$ and that $I_{\pm2}^{(z)}(t)$ reached its initial peak at $\bar{J}t_{\text{peak}}^{(I)}/2\pi \approx 1.22$, whereas $\mathcal{C}_z(t)$ reached its initial trough at $\bar{J}t_{\text{dip}}^{(e)}/2\pi \approx 2.37$. **a,b,** ×2π indicates that the x-axis coordinate equals the x-axis scale value multiplied by 2π.

comparisons between theory and experiment become particularly valuable. To this end, accurate calibration of the Hamiltonian parameters and high-quality data of the quantum dynamics with inevident decoherence are required. Here, by reaching consistency between experiment, approximate theory and numerical diagonalization, we revealed a few universal parameters and uncovered dominating interacting processes for this quench dynamics, which can be generalized to similar non-equilibrium dynamics in cold atoms, nitrogen-vacancy centres and other systems.

Online content

Any methods, additional references, Nature Portfolio reporting summaries, source data, extended data, supplementary information, acknowledgements, peer review information; details of author contributions and competing interests; and statements of data and code availability are available at https://doi.org/10.1038/s41567-024-02664-0.

References

1. Chin, C., Grimm, R., Julienne, P. & Tiesinga, E. Feshbach resonances in ultracold gases. *Rev. Mod. Phys.* **62**, 1225 (2010).
2. Pethick, C. J. & Smith, H. *Bose-Einstein Condensation in Dilute Gases* (Cambridge Univ. Press, 2008).
3. Sachdev, S. *Quantum Phase Transitions* (Cambridge Univ. Press, 2011).
4. Wei, D. et al. Quantum gas microscopy of Kardar-Parisi-Zhang superdiffusion. *Science* **376**, 716–720 (2022).
5. Geier, S. et al. Floquet Hamiltonian engineering of an isolated many-body spin system. *Science* **374**, 1149 (2021).
6. Gärttner, M. et al. Measuring out-of-time-order correlations and multiple quantum spectra in a trapped-ion quantum magnet. *Nat. Phys.* **13**, 781–786 (2017).
7. Joshi, M. K. et al. Observing emergent hydrodynamics in a long-range quantum magnet. *Science* **376**, 720–724 (2022).
8. Zu, C. et al. Emergent hydrodynamics in a strongly interacting dipolar spin ensemble. *Nature* **597**, 45–50 (2021).
9. Martin, L. S. et al. Controlling local thermalization dynamics in a Floquet-engineered dipolar ensemble. *Phys. Rev. Lett.* **130**, 210403 (2023).
10. Morgan, S. W., Fine, B. V. & Saam, B. Universal long-time behavior of nuclear spin decays in a solid. *Phys. Rev. Lett.* **101**, 067601 (2008).
11. Sorte, E. G., Fine, B. V. & Saam, B. Long-time behavior of nuclear spin decays in various lattices. *Phys. Rev. B* **83**, 064302 (2011).
12. Meier, B., Kohlrautz, J. & Haase, J. Eigenmodes in the long-time behavior of a coupled spin system measured with nuclear magnetic resonance. *Phys. Rev. Lett.* **108**, 177602 (2012).
13. Ramanathan, C., Cappellaro, P., Viola, L. & Cory, D. G. Experimental characterization of coherent magnetization transport in a one-dimensional spin system. *New J. Phys.* **13**, 103015 (2011).
14. Álvarez, G. A., Suter, D. & Kaiser, R. Localization-delocalization transition in the dynamics of dipolar-coupled nuclear spins. *Science* **349**, 846–848 (2015).
15. Li, J. et al. Measuring out-of-time-order correlators on a nuclear magnetic resonance quantum simulator. *Phys. Rev. X* **7**, 031011 (2017).
16. Rovny, J., Blum, R. L. & Barrett, S. E. Observation of discrete-time-crystal signatures in an ordered dipolar many-body system. *Phys. Rev. Lett.* **120**, 180603 (2018).
17. Wei, K. X., Ramanathan, C. & Cappellaro, P. Exploring localization in nuclear spin chains. *Phys. Rev. Lett.* **120**, 070501 (2018).
18. Wei, K. X. et al. Emergent prethermalization signatures in out-of-time ordered correlations. *Phys. Rev. Lett.* **123**, 090605 (2019).
19. Sánchez, C. M. et al. Perturbation independent decay of the Loschmidt echo in a many-body system. *Phys. Rev. Lett.* **124**, 030601 (2020).
20. Peng, P., Yin, C., Huang, X., Ramanathan, C. & Cappellaro, P. Floquet prethermalization in dipolar spin chains. *Nat. Phys.* **17**, 444–447 (2021).
21. Peng, P., Ye, B., Yao, N. Y. & Cappellaro, P. Exploiting disorder to probe spin and energy hydrodynamics. *Nat. Phys.* **19**, 1027–1032 (2023).
22. Fine, B. V. Long-time relaxation on spin lattice as a manifestation of chaotic dynamics. *Int. J. Mod. Phys. B* **18**, 1119–1159 (2004).
23. Fine, B. V. Long-time behavior of spin echo. *Phys. Rev. Lett.* **94**, 247601 (2005).
24. Zhang, R. & Zhai, H. Universal hypothesis of autocorrelation function from Krylov complexity. *Quantum Front.* **3**, 7 (2024).
25. Ljubotina, M., Žnidarič, M. & Prosen, T. Spin diffusion from an inhomogeneous quench in an integrable system. *Nat. Commun.* **8**, 16117 (2017).
26. Ljubotina, M., Žnidarič, M. & Prosen, T. Kardar-Parisi-Zhang physics in the quantum Heisenberg magnet. *Phys. Rev. Lett.* **122**, 210602 (2019).
27. Gopalakrishnan, S. & Vasseur, R. Kinetic theory of spin diffusion and superdiffusion in XXZ spin chains. *Phys. Rev. Lett.* **122**, 127202 (2019).
28. Gopalakrishnan, S., Vasseur, R. & Ware, B. Anomalous relaxation and the high-temperature structure factor of XXZ spin chains. *Proc. Natl Acad. Sci. USA.* **116**, 16250–16255 (2019).
29. Dupont, M. & Moore, J. E. Universal spin dynamics in infinite-temperature one-dimensional quantum magnets. *Phys. Rev. B* **101**, 121106 (2020).
30. Ljubotina, M., Desaules, J.-Y., Serbyn, M. & Papić, Z. Superdiffusive energy transport in kinetically constrained models. *Phys. Rev. X* **13**, 011033 (2023).
31. Roberts, D. A., Stanford, D. & Susskind, L. Localized shocks. *J. High Energy Phys.* **2015**, 51 (2015).
32. Parker, D. E., Cao, X., Avdoshkin, A., Scaffidi, T. & Altman, E. A universal operator growth hypothesis. *Phys. Rev. X* **9**, 041017 (2019).
33. Rufeil-Fiori, E., Sánchez, C. M., Oliva, F. Y., Pastawski, H. M. & Levstein, P. R. Effective one-body dynamics in multiple-quantum NMR experiments. *Phys. Rev. A* **79**, 032324 (2009).
34. Sánchez, C. M., Acosta, R. H., Levstein, P. R., Pastawski, H. M. & Chattah, A. K. Clustering and decoherence of correlated spins under double quantum dynamics. *Phys. Rev. A* **90**, 042122 (2014).
35. Álvarez, G. A. & Suter, D. NMR quantum simulation of localization effects induced by decoherence. *Phys. Rev. Lett.* **104**, 230403 (2010).
36. Resing, H. A. NMR relaxation in adamantane and hexamethylenetetramine: diffusion and rotation. *Mol. Cryst. Liq. Cryst.* **9**, 101–132 (1969).
37. McCall, D. W. & Douglass, D. C. Nuclear magnetic resonance in solid adamantane. *J. Chem. Phys.* **33**, 777–778 (1960).
38. Smith, G. W. On the calculation of second moments of nuclear magnetic resonance lines for large molecules. Adamantane molecule. *J. Chem. Phys.* **35**, 1134–1135 (1961).
39. Abragam, A. *The Principles of Nuclear Magnetism* (Oxford Univ. Press, 1961).
40. Suter, D., Liu, S. B., Baum, J. & Pines, A. Multiple quantum NMR excitation with a one-quantum Hamiltonian. *Chem. Phys.* **114**, 103–109 (1987).
41. Haeberlen, U. & Waugh, J. S. Coherent averaging effects in magnetic resonance. *Phys. Rev.* **175**, 453 (1968).
42. Deutsch, J. M. Eigenstate thermalization hypothesis. *Rep. Prog. Phys.* **81**, 082001 (2018).
43. Mori, T., Kuwahara, T. & Saito, K. Rigorous bound on energy absorption and generic relaxation in periodically driven quantum systems. *Phys. Rev. Lett.* **116**, 120401 (2016).
44. Abanin, D. A., De Roeck, W., Ho, W. W. & Huveneers, F. Effective Hamiltonians, prethermalization, and slow energy absorption in periodically driven many-body systems. *Phys. Rev. B* **95**, 014112 (2017).
45. Zhou, T. G., Zheng, W. & Zhang, P. Universal aspect of relaxation dynamics in random spin models. Preprint at https://doi.org/10.48550/arXiv.2305.02359 (2023).
46. Konoplya, R. A. & Zhidenko, A. Quasinormal modes of black holes: from astrophysics to string theory. *Rev. Mod. Phys.* **83**, 793–836 (2011).

47. Witczak-Krempa, W. & Sachdev, S. Quasinormal modes of quantum criticality. *Phys. Rev. B* **86**, 235115 (2012).
48. Shankar, R. Renormalization-group approach to interacting fermions. *Rev. Mod. Phys.* **66**, 129 (1994).
49. Sachdev, S. & Ye, J. Gapless spin-fluid ground state in a random quantum Heisenberg magnet. *Phys. Rev. Lett.* **70**, 3339 (1993).
50. Kitaev, A. A simple model of quantum holography (part 2). Talk at the Kavli Institute for Theoretical Physics, University of California, Santa Barbara https://online.kitp.ucsb.edu/online/entangled15/kitaev2/ (2015).
51. Maldacena, J. & Stanford, D. Remarks on the Sachdev-Ye-Kitaev model. *Phys. Rev. D* **94**, 106002 (2016).
52. Chowdhury, D., Georges, A., Parcollet, O. & Sachdev, S. Sachdev-Ye-Kitaev models and beyond: window into non-Fermi liquids. *Rev. Mod. Phys.* **94**, 035004 (2022).
53. Aue, W. P., Bartholdi, E. & Ernst, R. R. Two dimensional spectroscopy. Application to nuclear magnetic resonance. *J. Chem. Phys.* **64**, 2229–2246 (1976).
54. Wokaun, A. & Ernst, R. R. Selective detection of multiple quantum transitions in NMR by two-dimensional spectroscopy. *Chem. Phys. Lett.* **52**, 407–412 (1977).
55. Drobny, G., Pines, A., Sinton, S., Weitekamp, D. P. & Wemmer, D. Fourier transform multiple quantum nuclear magnetic resonance. *Faraday Symp. Chem. Soc.* **13**, 49 (1978).
56. Bodenhausen, G. Multiple-quantum NMR. *Prog. Nucl. Magn. Reson. Spectrosc.* **14**, 137–173 (1980).
57. Yen, Y. & Pines, A. Multiple quantum NMR in solids. *J. Chem. Phys.* **78**, 3579–3582 (1983).
58. Baum, J., Munowitz, M., Garroway, A. N. & Pines, A. Multiple quantum dynamics in solid state NMR. *J. Chem. Phys.* **83**, 2015–2025 (1985).
59. Gärttner, M., Hauke, P. & Rey, A. M. Relating out-of-time-order correlations to entanglement via multiple-quantum coherences. *Phys. Rev. Lett.* **120**, 040402 (2018).
60. Larkin, A. I. & Ovchinnikov, Y. N. Quasiclassical method in the theory of superconductivity. *Sov. Phys. JETP* **28**, 1200–1205 (1969).
61. Shenker, S. H. & Stanford, D. Multiple shocks. *J. High Energy Phys.* **2014**, 46 (2014).
62. Kitaev, A. Hidden correlations in the Hawking radiation and thermal noise. Talk given at the Fundamental Physics Prize Symposium. *Kavli Institute for Theoretical Physics* https://online.kitp.ucsb.edu/online/joint98/kitaev/ (2014).
63. Maldacena, J., Shenker, S. H. & Stanford, D. A bound on chaos. *J. High Energy Phys.* **2016**, 106 (2016).
64. Hosur, P., Qi, X.-L., Roberts, D. A. & Yoshida, B. Chaos in quantum channels. *J. High Energy Phys.* **2016**, 4 (2016).
65. Landsman, K. A. et al. Verified quantum information scrambling. *Nature* **567**, 61 (2019).

Methods

Hamiltonian engineering

By periodically applying the RF pulse sequence to the natural dipolar Hamiltonian, we could engineer the desired form of the anisotropic Heisenberg models of equation (4) as an effective time-independent Hamiltonian by the average Hamiltonian theory[41]. The basic building block of the RF pulse train is an eight-pulse sequence, which was initially introduced to study MQCs[40]. Explicitly, the eight-pulse sequence is represented as follows:

$$(\tau_z, \mathbf{x}, \tau_y, \mathbf{y}, 2\tau_x, \mathbf{y}, \tau_y, \mathbf{x}, 2\tau_z, \mathbf{x}, \tau_y, \mathbf{y}, 2\tau_x, \mathbf{y}, \tau_y, \mathbf{x}, \tau_z),$$

where $\mathbf{x}$ and $\mathbf{y}$ denote the RF pulses that induce collective $\pi/2$ rotations along the $\hat{x}$ and $\hat{y}$ directions, respectively. By adjusting the pulse intervals τ_α such that $\tau_\alpha = [1 + \xi_\alpha]\tau$, we can realize different configurations of the anisotropic parameters (ξ_x, ξ_y, ξ_z) to the leading order of the Magnus expansion[66].

Hamiltonian calibration

We calibrated the actually realized anisotropic parameters (ξ'_x, ξ'_y, ξ'_z) and the weight of residual terms other than $\hat{S}_{ia}^\alpha \hat{S}_{jb}^\alpha$ in the effective Floquet Hamiltonian $\hat{H}_F$. We employed the Floquet prethermalization hypothesis[43,44], which assumes that the system attains a quasi-stationary state $\hat{\rho}_{pre}$, approximately characterized by a canonical ensemble associated with the effective Hamiltonian $\hat{H}_F$ before being heated to infinite temperature. We then have

$$\hat{\rho}_{pre} \approx \frac{e^{-\beta_{eff}\hat{H}_F}}{\mathrm{Tr}\,(e^{-\beta_{eff}\hat{H}_F})} \propto \mathbb{1} - \beta_{eff}\hat{H}_F, \qquad (9)$$

where β_{eff} represents the effective inverse temperature, which is determined by the initial state $\hat{\rho}_0$ through energy conservation $\mathrm{Tr}(\hat{\rho}_0\hat{H}_F) = \mathrm{Tr}(\hat{\rho}_{pre}\hat{H}_F)$. The Floquet prethermalization has been experimentally demonstrated in spin chains with dipolar interactions[18,20].

As elaborated in the Supplementary Information, we initially prepared states with finite inverse spin temperatures and then allowed them to prethermalize under the $\hat{H}$ of equation (4) with various anisotropic configurations for a time period of $\bar{J}t \geq 14\pi$. In addition, we prepared dipolar-ordered states[67,68] as a reference state using the Jeener–Broekaert method[67]. The traceless components of the density matrix of these states are given by

$$\delta\hat{\rho}_x^D \propto \sum_{i \neq j, ab} J_{ij}\left(-\hat{S}_{ia}^y\hat{S}_{jb}^y - \hat{S}_{ia}^z\hat{S}_{jb}^z + 2\hat{S}_{ia}^x\hat{S}_{jb}^x\right), \qquad (10)$$

and the other two dipolar-ordered states $\delta\hat{\rho}_y^D$ and $\delta\hat{\rho}_z^D$ can be determined through cyclic permutations. In the experiment, we measured the inner products between the prethermal state and each of the dipolar-ordered states. These inner products are proportional to the anisotropic parameters:

$$\mathrm{Tr}\left(\hat{\rho}_{pre}\delta\hat{\rho}_x^D\right) \propto (2\xi'_x - \xi'_y - \xi'_z)\sum_{i \neq j, ab} J_{ij}^2 \propto \xi'_x. \qquad (11)$$

Similarly, we found that $\mathrm{Tr}(\hat{\rho}_{pre}\delta\hat{\rho}_y^D) \propto \xi'_y$ and $\mathrm{Tr}(\hat{\rho}_{pre}\delta\hat{\rho}_z^D) \propto \xi'_z$. This determines the actual anisotropic parameters (ξ'_x, ξ'_y, ξ'_z). The discrepancies between these parameters and their target values (ξ_x, ξ_y, ξ_z) are quantified by $\Delta \equiv |\boldsymbol{\xi}' - \boldsymbol{\xi}|/|\boldsymbol{\xi}|$. Throughout all the realized configurations, the values of Δ were calibrated to be within 3% (Supplementary Note 4).

The weight of the residual terms, denoted as $\cdots$ in the overall effective Hamiltonian of equation (4), is defined by $\varepsilon \equiv \sqrt{\mathrm{Tr}(\cdots^2)/\mathrm{Tr}(\hat{H}^2)}$. It primarily leverages the orthogonal relationships between the residual term in the prethermal states $\hat{\rho}_{pre}$ and the dipolar-ordered states $\delta\hat{\rho}_\alpha^D$ and incorporates more inner product measurements. The values of ε were determined to be less than 20% across all the realized configurations (Supplementary Note 4).

Exact diagonalization

In the exact-diagonalization calculations, we were restricted to a simplified model consisting of a single spin-1/2 on each molecule with system size up to $N = 8$. The Hamiltonian is

$$\hat{H}_{ED} = \sum_{i<j} J_{ij}\left(\xi_x\hat{S}_i^x\hat{S}_j^x + \xi_y\hat{S}_i^y\hat{S}_j^y + \xi_z\hat{S}_i^z\hat{S}_j^z\right), \qquad (12)$$

where J_{ij} is modelled as a random variable obeying a normal distribution $J_{ij} \sim \mathcal{N}[0, (2J/\sqrt{N})^2]$. For each disorder realization of J_{ij}, we prepared the initial state as a thermal density matrix, denoted as $\hat{\rho} \propto \exp(-\beta(\hat{H}_{ED} + \delta\hat{H}))$, where $\beta = \hbar/(k_BT)$ denotes the inverse temperature. We introduced an external polarization field $\delta\hat{H} = -g\sum_i \hat{S}_i^x$. We fixed $\beta J = 0.2$ and $g/J = 2$, as explained in 'Parameters in the numerical simulations'. The system was then allowed to evolve under the Hamiltonian of equation (12), and the result was averaged over 10^3 random realizations.

Large-M expansion

We transformed the randomly interacting spin model of equation (4) into a theory of randomly interacting fermions by adopting the Abrikosov fermion representation. In this representation, the spin operators are expressed as $\hat{S}_{ia}^\alpha = \frac{1}{2}\sum_{ss'} \hat{c}_{ia,s}^\dagger(\sigma^\alpha)_{ss'}\hat{c}_{ia,s'}$ $(s,s' =\uparrow,\downarrow)$, limited to the single occupation subspace. Our main interest lies in the spin polarization dynamics, which can be expressed as $\langle\hat{O}_x(t)\rangle = -iN(G_{\uparrow\downarrow}^>(t,t) + G_{\downarrow\uparrow}^>(t,t))/2$. Here the real-time Green's functions are defined as $G_{ss'}^>(t_1, t_2) \equiv -i\langle c_{ia,s}(t_1)c_{ia,s'}^\dagger(t_2)\rangle$ and $G_{ss'}^<(t_1, t_2) \equiv i\langle c_{ia,s'}^\dagger(t_2)c_{ia,s}(t_1)\rangle$. The evolution of these Green's functions can be described by a set of classical equations, commonly known as the Kadanoff–Baym equation:

$$\begin{aligned} i\partial_{t_1}G^\gtrless &= \Sigma^R \circ G^\gtrless + \Sigma^\gtrless \circ G^A, \\ -i\partial_{t_2}G^\gtrless &= G^R \circ \Sigma^\gtrless + G^\gtrless \circ \Sigma^A, \end{aligned} \qquad (13)$$

where $G^{R/A}$ are the retarded and advanced Green's functions. $\Sigma^\gtrless$ and $\Sigma^{R/A}$ represent the real-time self-energies, which satisfy $\Sigma^{R/A} = \pm\Theta(\pm t_{12})(\Sigma^> - \Sigma^<)$. To make further theoretical advances, an $\mathrm{SU}(M) \times \mathrm{SU}(2)$ generalization was introduced, which is like the approach used in refs. 45,69. By taking both the large-N and the large-M limit, melon diagrams play a dominant role in the self-energies, as in the Sachdev–Ye–Kitaev model. This leads to

$$\Sigma^\gtrless(t_1, t_2) = \frac{J^2}{4}\sum_{\alpha,\alpha'} \xi_\alpha\xi_{\alpha'}\sigma^\alpha G^\gtrless(t_1,t_2)\sigma^\alpha \mathrm{Tr}\left[\sigma^{\alpha'}G^\gtrless(t_1,t_2)\sigma^\alpha G^\lessgtr(t_2,t_1)\right]. \qquad (14)$$

Numerically, we prepared the system in an initial state described by a thermal ensemble at $\beta J = 0.2$ with a polarization field $g/J = 2$. The corresponding initial Green's functions were obtained through iterations. Subsequently, we evolved $G^\gtrless$ by combining equation (13) and equation (14) to determine $\langle\hat{O}_x(t)\rangle$. Besides, by conducting a quasinormal mode analysis, one can analytically derive the long-time spin relaxation dynamics of equation (7) within the large-M approximation[45]. This calculation is elaborated in the Supplementary Information.

Mean-field theory

Another theoretical scheme for analysing randomly interacting spin models is the mean-field theory. Here, we introduce the average polarization on each molecule as $\hat{M}_i^\alpha = \frac{1}{N_a}\sum_a \hat{S}_{ia}^\alpha$. Due to the statistical averaging, we expected the fluctuation of $\hat{M}_i^\alpha$ to be small, allowing us to approximate it as a classical vector M_i^α. The Heisenberg equation for $\hat{M}$ then becomes

$$\frac{dM_i^\alpha}{dt} = N_a\sum_{j,\beta\gamma} J_{ij}\epsilon^{\alpha\beta\gamma}\xi_\beta M_j^\beta M_i^\gamma. \qquad (15)$$

In the numerical simulation, we investigated a system with 2×10^3 molecules. The initial configuration of M_i^α was randomly generated using an independent Gaussian distribution, with mean $\overline{\mathbf{M}_i} = \left(\frac{\beta g}{4}, 0, 0\right)$, $\beta g = 0.4$ and variance $\overline{(\delta M_i^\alpha)^2} = 1/(4N_a)$. Subsequently, we evolved M_i^α according to equation (15) for each random realization and computed $\langle \hat{O}^\alpha \rangle = N_a \sum_i M_i^\alpha$. The final result was then averaged over 20 independent simulations.

Parameters in the numerical simulations

The NMR experiment was conducted at room temperature, necessitating the conditions $\beta J \ll 1$ and $\beta g \ll 1$. Additionally, the external magnetic field strongly polarized the state, so that the initial state could be approximated by $\hat{\rho} \propto \exp\left(-\beta\hat{H}_{\mathrm{dip}} + \beta g \sum_{ia} \hat{S}_{ia}^\alpha\right) \approx \mathbb{1} + \beta g \sum_{ia} \hat{S}_{ia}^\alpha$. This required that the magnitude of the external field must be substantially larger than the characteristic strength of the dipolar interaction $\hat{H}_{\mathrm{dip}}$ (equation (3)), that is, $g/J \gg 1$. All the parameters in the numerical simulations satisfied these conditions. In the Supplementary Information, we demonstrate that a moderate change of parameters yields qualitatively similar results. In particular, the oscillation frequencies and decay rates remain independent of β and g.

Data availability

Source data are provided with this paper. The data used in this research are also available at https://github.com/tgzhou98/Quench-Random-Spin and https://github.com/lyuchen96/Quench-Random-Spin. The data for Fig. 3 are available at the first site, whereas the second site provides the data for Figs. 1, 2 and 4 and for the Supplementary Information. Further data are available from the corresponding authors upon reasonable request.

Code availability

The code used to produce Fig. 3 is available at https://github.com/tgzhou98/Quench-Random-Spin, which contains three packages of numerical simulations and one package for fitting and the corresponding error bar analysis. The code used for Figs. 1, 2 and 4 and for the Supplementary Information is available at https://github.com/lyuchen96/Quench-Random-Spin.

References

66. Magnus, W. On the exponential solution of differential equations for a linear operator. *Commun. Pure Appl. Math.* **7**, 649–673 (1954).
67. Jeener, J. & Broekaert, P. Nuclear magnetic resonance in solids: thermodynamic effects of a pair of RF pulses. *Phys. Rev.* **157**, 232–240 (1967).
68. Cho, H., Cory, D. G. & Ramanathan, C. Spin counting experiments in the dipolar-ordered state. *J. Chem. Phys.* **118**, 3686–3691 (2003).
69. Zhou, T. G., Pan, L., Chen, Y., Zhang, P. & Zhai, H. Disconnecting a traversable wormhole: universal quench dynamics in random spin models. *Phys. Rev. Res.* **3**, L022024 (2021).

Author contributions

Y.L., Z.W. and X.P. designed the experimental protocol. Y.L. performed the measurements. P.P., S.Z. and R.F. assisted with the experiments and numerical simulations. T.G.Z., R.Z., W.Z., P.Z. and H.Z. developed the theory. H.Z., X.P. and J.D. supervised the project. All authors contributed to analysing the data, discussing the results and writing the manuscript.

Competing interests

The authors declare no competing interests.

Additional information

Supplementary information The online version contains supplementary material available at https://doi.org/10.1038/s41567-024-02664-0.

Correspondence and requests for materials should be addressed to Pengfei Zhang, Hui Zhai or Xinhua Peng.

Peer review information *Nature Physics* thanks the anonymous reviewers for their contribution to the peer review of this work.

Reprints and permissions information is available at www.nature.com/reprints.